University of Groningen

Iron-substituted cubic silsesquioxane pillared clays

Potsi, Georgia; Ladavos, Athanasios K.; Petrakis, Dimitrios; Douvalis, Alexios P.; Sanakis, Yiannis; Katsiotis, Marios S.; Papavassiliou, Georgios; Alhassan, Saeed; Gournis, Dimitrios; Rudolf, Petra

IMPORTANT NOTE: You are advised to consult the publisher's version (publisher's PDF) if you wish to cite from it. Please check the document version below.

Document Version
Publisher's PDF, also known as Version of record

Link to publication in University of Groningen/UMCG research database
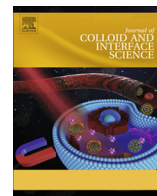
Regular Article

Iron-substituted cubic silsesquioxane pillared clays: Synthesis, characterization and acid catalytic activity

Georgia Potsi [a,b], Athanasios K. Ladavos [c], Dimitrios Petrakis [d], Alexios P. Douvalis [e], Yiannis Sanakis [f], Marios S. Katsiotis [g], Georgios Papavassiliou [f], Saeed Alhassan [g], Dimitrios Gournis [a,*], Petra Rudolf [b,*]

[a] Department of Materials Science & Engineering, University of Ioannina, 45110 Ioannina, Greece
[b] Zernike Institute for Advanced Materials, University of Groningen, Nijenborgh 4, 9747 AG Groningen, The Netherlands
[c] School of Natural Resources and Enterprise Management, University of Patras, Agrinio 30100, Greece
[d] Department of Chemistry, University of Ioannina, 45110 Ioannina, Greece
[e] Physics Department, University of Ioannina, 45110 Ioannina, Greece
[f] Institute of Nanoscience and Nanotechnology, NCSR "DEMOKRITOS", 15310 Ag. Paraskevi-Attikis, Athens, Greece
[g] Department of Chemical Engineering, The Petroleum Institute, PO Box 2533, Abu Dhabi, United Arab Emirates

GRAPHICAL ABSTRACT
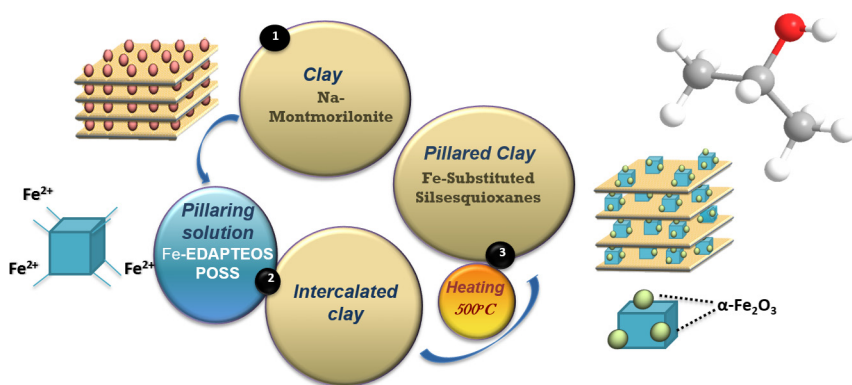
ARTICLE INFO

ABSTRACT

Novel pillared structures were developed from the intercalation of iron-substituted cubic silsesquioxanes in a sodium and an acid-activated montmorillonite nanoclay and evaluated as acid catalysts. Octameric cubic oligosiloxanes were formed upon controlled hydrolytic polycondensation of the corresponding monomer (a diamino-alkoxysilane) and reacted with iron cations to form complexes that were intercalated within the layered nanoclay matrices. Upon calcination iron oxide nanoparticles are formed which are located on the silica cubes (pillars) and on the surfaces of the clay platelets. Acid activation of the nanoclay was performed in order to increase the number of acid active sites in the pristine clay and thus increase its catalytic activity. A plethora of analytical techniques including X-ray diffraction, thermal analyses, Fourier transform infrared, electron paramagnetic resonance, Raman, Mössbauer and X-ray photoelectron spectroscopies and porosimetry measurements were used in order to follow the synthesis

---

steps and to fully characterize the final catalysts. The resulting pillared clays exhibit a high specific area and show significant acid catalytic activity that was verified using the catalytic dehydration of isopropanol as a probe reaction.

1. Introduction

The field of engineering nanomaterials has a continuing need of well-defined building blocks that imbue functionality and allow for nanoparticle-by-nanoparticle assembly of a wide variety of materials with precise control over the nanoarchitecture [1,2]. Silsesquioxanes possess a pronounced aptitude to form three dimensional cage-like highly symmetric frameworks known as polyhedral oligosilsesquioxanes (POSS) with cubic, hexagonal, octagonal, decagonal, dodecagonal or even open cage-like morphology [3–5]. Cubic silsesquioxanes (cubes), synthesized from the hydrolytic condensation of the corresponding trifunctional organo-silicon monomers, is the most common polyhedral structure and provide the opportunity to design and "construct" materials with extremely well-defined dimensions and behaviour [3–13] In this context, cubic silsesquioxanes of the type $X_8Si_8O_{12}$ where X is $-(CH_2)_3NH_2$, $-(CH_2)_3NR_2$ and $-(CH_2)_3NH(CH_2)_2NH_2$ have been successfully employed as precursor reagents for pillaring inorganic layered solids such as clays[14–19], metal (IV) hydrogen phosphates [20–22], photonic titanoniobates [23], graphenes and graphene oxide [3,24–26], graphene oxide nanoribbons [27], halloysite nanotubes [28] and perovskites [29]. Protonation of the amino groups generates oligomeric cationic species with expendable and bulky organic groups that can easily be inserted into the interlayer space of a phyllomorphous clay in amounts exceeding the cation exchange capacity of the mineral and can successively be removed by thermal treatment, resulting in silica pillared structures [15,14]. This excess being in the form of physically adsorbed ion pairs influences the free distance between the layers and the surface area as well as the porosity of the silica-pillared composites.

On the other hand, these various mono- or bi-functional aminosilanes possess the ability to bind metal ions, M^{n+} (*e.g.* Cu^{2+}, Ni^{2+}, Co^{2+}, Fe^{3+}, Al^{3+}), yielding metal complexes, $M_x{}^{n+}[X_8Si_8O_{12}]_y$, and thus enabling the design and synthesis of metal complexes in which the redox active metal center is coordinated to the functionalized group of the siloxane octamer [22]. In particular, amino-functionalized POSS structures constitute high affinity metal-binding sites; where the metal ions are bound in a single ligand (monodentate) via the amino group, thus resulting in a maximization of metal binding efficiency [30]. The resulting cationic complexes are expected to be excellent pillaring precursors and may be further calcined to remove the organic side arms and produce cross-linked metal-substituted silica-pillared clays of high porosity and thermal stability. Upon calcination the metal ions may retain isolated as metal oxides located on both the clay surface and the pillar or may be integrated into the silica pillar. The clays pillared with metal oxide silica are solid acids with moderate or high Brønsted and Lewis acidity originating from acid sites located on the pillars and the clay surface; they can be used as acid catalysts in the range 100–600 °C, in which most catalytic reactions take place. Isopropyl alcohol decomposition is one example of a specific reaction where this type of pillared clay can be used as efficient catalyst. Furthermore the use of acid-activated clays instead of sodium-intercalated ones as efficient substrates for the synthesis of pillared structures could enhance the acid properties and subsequently their catalytic activity [31–36].

The first attempt to intercalate metal POSS in pillared structures was performed by Khattou et al. [37,38] who intercalated a Cu^{2+}-octa(diaminoalkyl) siloxane complex into a-zirconium phosphate and examined the pillaring materials obtained after calcination by electron paramagnetic resonance (EPR) spectroscopy. In this case the metal ions act as probe for the determination of the evolution of local symmetry and structure during the pillaring process when using an element specific technique. More recently Carniato et al.[39] demonstrated the intercalation of a bifunctional protonated titanium-containing aminopropyl isobutyl POSS, within the interlayer space of a synthetic sodium saponite and its use as filler in a polystyrene-based nanocomposite designed to enhance the thermooxidative properties. The same group [40] also intercalated Ti-containing aminopropylisobutyl polyhedral oligomeric silsesquioxane in synthetic saponite and investigated the catalytic activity of this composite in cyclohexene oxidation. Other catalysts based on clay-POSS hybrids include synthetic laponite clay first modified by octaaminopropyl polyhedral oligomeric silsesquioxane and then used to support a nickel alpha-diimine late-transition-metal catalyst for ethylene polymerization [41]; laponite and montmorillonite functionalized with (3-aminopropyl)triethoxysilane and use both as supports for the vanadyl(IV) acetylacetonate catalysis [42] and POSS intercalated bentonites[30] for metal up take of copper, cadmium and lead.

In this work we report the intercalation of Fe^{3+}-substituted cubic silsesquioxanes in a sodium and an acid-activated montmorillonite to form novel catalytic pillared structures. Iron was chosen as metal catalyst because of its low toxicity and high abundance that make it attractive for potential industrial applications [43]. A plethora of analytical techniques including X-ray diffraction (XRD), thermal analyses (DTA/TGA), Fourier transform infrared (FTIR), electron paramagnetic resonance (EPR), Raman, Mössbauer and X-ray photoelectron (XPS) spectroscopies and porosimetry measurements were used in order to follow the synthesis steps and to fully characterize the final catalysts. The resulting pillared clays exhibit a high specific area and a narrow pore size distribution; they show a significant acid catalytic activity in the isopropanol decomposition that was used as a probe reaction.

2. Experimental section

2.1. Materials and reactions

The clay used in this study was a natural Texas montmorillonite, STx-1 (**Na-T**) with a cation exchange capacity (CEC) equal to 80 mequiv/100 g clay and particle size ≤2 μm, obtained from the Source Clay Minerals Repository at the University of Missuri, Columbia. It was purified following well established procedures in clay science [44]. Sodium exchanged samples were prepared by immersing the clay into 1 N solution of sodium chloride. Cation exchange was completed by washing and centrifuging four times with a dilute solution of NaCl. The samples were finally washed with distilled-deionized water and transfer into dialysis tubes in order to obtain chloride free clays and finally dried at room temperature.

For the preparation of acid-activated-clay (**HT**), Na^+-montmorillonite (50.0 g) were ground and magnetically stirred

with 250 mL of 2 M H_2SO_4 (from Riedel-deHaen) at 80 °C for 2 h in a round-bottom flask. The slurry was cooled in air, centrifuged and washed with distilled water and the operation was repeated twice. The sample contained in a dialysis membrane was placed in deionized water and the water was renewed until the pH was neutral and the conductivity was stable [45,46]. The sample was finally dried at room temperature.

The organosilane used in this study was 3-(2-aminoethylamino)-propyltrimethoxysilane, (EDAPTMOS), $H_2N(CH_3)_2NH(CH_2)_3$-$Si(OCH_3)_3$, from Fluka Chemicals. The formation of the octameric oligosiloxane from the hydrolytic polycondensation of the monomer occurs after dilution of EDAPTMOS in ethanol–water (v/v = 14/1) to give a solution of concentration 0.45 M [15,22,21]. 30 mL of an aqueous 0.1 M $FeCl_2$ solution (3 mmol) was reacted with 20 mL of the above solution (9 mmol) upon stirring. The colour of the ferrous chloride solution changed from pale orange to dark green indicative of the complexation of ferrous cations with the amino functional group of the corresponding siloxane molecules. The produced Fe-EDAPTMOS complex was used immediately after its formation in order to avoid oxidation of ferrous cations before the intercalation into the clay platelets.

The Fe-EDAPTMOS-clay complexes were prepared by reacting, under stirring, a 0.5% wt clay suspension with aliquots of the above siloxane complex solution such that the ratio, R = [Fe-EDAPTMOS]/[clay], was 3. The colour of the slurry changed gradually within 1 h after the addition of iron-complex from green to orange, which indicates the oxidation of Fe(II) to Fe(III). After stirring for 6 h, the clay-organosilane aggregates were washed with water five times, separated by centrifugation and air dried by spreading on glass plates. In order to prepare the pillared clays, the intercalated with the Fe-EDAPTMOS clay samples were calcined in air at 500 °C for 3 h. Two intercalated clay samples and the corresponding pillared structures, produced upon calcination, were prepared using the raw and the acid activated montmorillonite denoted as **TFeED**, **HTFeED**, **TFeED-500** and **HTFeED-500**.

2.2. X-ray diffraction measurements

X-ray powder diffraction data were collected on a D8 Advance Bruker diffractometer by using CuK_α (40 kV, 40 mA) radiation and a secondary beam graphite monochromator. The patterns were recorded in the 2-theta (2Θ) range from 2° to 80°, in steps of 0.02° and a counting time 2 s per step.

2.3. FTIR spectroscopy

Infrared spectra in the region of 400–4000 cm^{-1} were measured with a SHIMADZU 8400 infrared spectrometer equipped with a DTGS detector. Each spectrum was the average of 200 scans collected at 2 cm^{-1} resolution by means a SPECAC variable-angle attachment. Samples were in the form of KBr pellets containing *ca.* 2 wt% sample.

2.4. Electron paramagnetic resonance (EPR) spectroscopy

The EPR spectra were obtained using a Bruker ER 200D-SRC spectrometer equipped with an Oxford ESR 9 cryostat, a Bruker 035 M NMR-gaussmeter and an Anritsu MF76A microwave frequency counter. All spectra were recorded under the following conditions: modulation amplitude MA = 2 Gpp, microwave power MP = 6.3 mW and temperature T = 300 K.

2.4.1. [57]Fe-Mössbauer spectroscopy

[57]Fe Mössbauer spectra (MS) were collected at room temperature (RT = 300 K) and 10 K, using constant acceleration spectrometers,

equipped with a [57]Co(Rh) sources kept at RT and a closed loop He (ARS) Mössbauer cryostat. Calibration of the spectrometers was done using metallic α-Fe at RT and all isomer shift (IS) values are reported relative to this standard. The fitting of the recorded MS was done using the IMSG code [47].

2.5. X-ray photoelectron spectroscopy (XPS)

For the XPS measurements, samples were introduced via a load-lock system into a SSX-100 (Surface Science Instruments) photoelectron spectrometer with a monochromatic Al Kα X-ray source (hν = 1486.6 eV). The base pressure in the spectrometer was 2×10^{-9} Torr during measurements. The energy resolution was set to 1.6 eV; the photoelectron take off angle was 37° with respect to the surface normal. An electron flood gun providing 0.1 eV kinetic energy electrons was used to compensate for sample charging. Samples were prepared by drop casting onto gold substrates. Binding energies were referenced to the C1s core level of the C—C bond set to the nominal value of 284.8 eV [48]. Spectral analysis included a Shirley or linear background subtraction and peak deconvolution employing mixed Gaussian−Lorentzian functions, in a least squares curve-fitting program (WinSpec) developed at the LISE, University of Namur, Belgium. When more than one component was used to fit a core level photoemission line, binding energies are reported ±0.1 eV.

2.6. DTA/TGA measurements

Thermogravimetric (TGA) and differential thermal (DTA) analyses were performed using a Shimadzu DTG 60 Thermal Analyzer. Samples of approximately 15 mg were heated in air from 25 to 600 °C, at a rate of 10 °C/min.

2.7. Surface area and porosity measurements

The surface area and pore volume of the samples were determined by a SORPTOMATIC 1900 volumetric adsorption-desorption apparatus, using nitrogen as adsorbent at 77 K. Prior to the determination of the adsorption-desorption isotherms the samples were degassed at 200 °C in vacuum of 5×10^{-2} mbar for 20 h. The specific surface area of the samples was calculated by applying the BET equation using the linear part (0.05 < P/P_o < 0.15) of the adsorption isotherm and assuming a closely packed BET monolayer, with $\alpha_m(N_2)$ = 0.162 nm^2 at 77 K.

2.8. Catalytic measurements

The catalytic decomposition of isopropanol was performed in a bench-scale flow reactor with a 1 cm diameter silica tube housing a sealed-in quartz bed onto which 0.20 g of the catalyst was placed. The system was heated in a tubular furnace with a temperature control system that stabilizes the temperature within ±1 °C. Analyses of reactants and products were carried out by sampling 1 cm^3 of the gases in a Fisons GC-9130 gas chromatograph equipped with a flame ionization detector. The column used for analysis was a DB-WAX, 30 m x 0.32 mm, and with film thickness 0.5 µm, supplied by J&W scientific. Helium was used as carrier gas in the gas chromatograph. Another line admitted Helium through a saturator bottle (40 ± 1 cm^3 min^{-1}) containing the isopropanol (at constant temperature), so that the isopropanol vapour was driven into the reactor. Under the experimental conditions the partial pressure of isopropanol was 33 mmHg. Measurements were taken in the range of 90–200 °C in 5 or 10 °C intervals. Before the catalytic experiments were started the catalyst was heated at 500 °C for 2 h under Helium flow to remove adsorbed water from the pores. No signs of catalyst 'die off' were observed during the time scale of our

experiments. The products detected were propene, diisopropyl ether and water. From the percentage degree of total conversion of isopropanol we calculated the reaction rate at each reaction temperature. Moreover the selectivity for each main product, propene and diisopropyl ether, at various degrees of total conversion of isopropanol was also determined.

3. Results and discussion

3.1. Synthetic pathway

For the development of the catalytic pillared clays, a sodium montmorillonite (Na-T) and its acid activated form (HT) were used. Acid activation was performed in order to increase the number of acid active sites in the pristine clays and thus increase its catalytic activity during the dehydration of the isopropanol, which is an acid catalyzed reaction. For the pillaring solution, octameric cubic oligosiloxanes were formed upon controlled hydrolytic polycondensation of the corresponding monomer (EDAPTMOS) in an ethanol-water mixture and immediately reacted with ferrous cations to form complexes of the type $Fe_x^{2+}[X_8Si_8O_{12}]_y$. The colour of the solution changed from pale orange to dark green, indicative of the complexation of ferrous cations with the amino functional group of the corresponding siloxane molecules. When the pillaring solution was added to an aqueous dispersion of the clay an immediate flocculation of clay particles was observed due to the insertion of complex in the clay galleries by ion exchange. The colour of the slurry changed gradually within 1 h after the addition of iron-complex from green to orange, pointing to the oxidation of Fe(II) to Fe(III). Finally, intercalated samples were calcined at 500 °C in air to obtain pillared clays. The calcination procedure contributes to the removal of the organic chains of the organo-silane cubes and to the creation of iron oxide nanoparticles, which are immobilized on the silica cubes and on the surfaces of the clay platelets. A schematic representation of the experimental procedure is depicted in Fig. 1.

3.2. X-ray diffraction analysis

X-ray diffraction was employed to reveal the successful intercalation of iron-silsesquioxane complexes as well as the formation of the pillared structures [44]. The XRD patterns of intercalated samples (for both Na-T and HT clays) before and after calcination at 500 °C are displayed in Fig. 2. The insertion of iron-silsesquioxane complexes between the aluminosilicate layers increases the interlayer distance. More specifically, for TFeED obtained by intercalation in Na-T clay, the basal d_{001}-spacing, which is 12.6 Å in the initial montmorillonite clay, becomes 18.2 Å after the modification; this corresponds to an interlayer separation of 18.2–9.6 = 8.6 Å, where 9.6 Å represents the thickness of a clay layer [44,49]. This value is reasonable if we consider that the edge of the siloxane cube (Si—O—Si distance) is 6.0 Å [14] and, due to complexation with the ferric cations, the flexible organic chains adopt a inclined orientation between the clay layers. Moreover, the interlayer distance of 8.6 Å is actually higher compared to the one observed (7.1 Å) upon clay intercalation with this particular aminosiloxane not complexed with ferric cations [30]. Similar results were obtained for the acid-activated montmorillonite. The XRD pattern of the HTFeED sample (Fig. 2b) shows a d_{001} spacing of 17.2 Å, which corresponds to an interlayer separation of 7.6 Å. The interlayer distance in this case is slightly lower than for TFeED. However, a similar geometrical arrangement must be adopted in this case too with the flexible side chains of the siloxane cubes in an inclined orientation with respect to the aluminosilicate platelets. Upon calcination at 500 °C, the d_{001} spacing was decreased to 16.3 and 15.4 Å, for TFeED-500 and HTFeED-500 respectively, indicative of the removal of the side organic groups of the siloxane cubes and the subsequent reduction in the interlayer distance. Moreover, the absence of reflection peaks of the crystalline phase of iron oxides (not shown below, see supporting information)) in the 2Θ region 2–80° indicates that iron oxide nanoparticles produced upon calcination are small enough and are not aggregated on the external clay surfaces but rather homogeneously dispersed in the clay matrix.
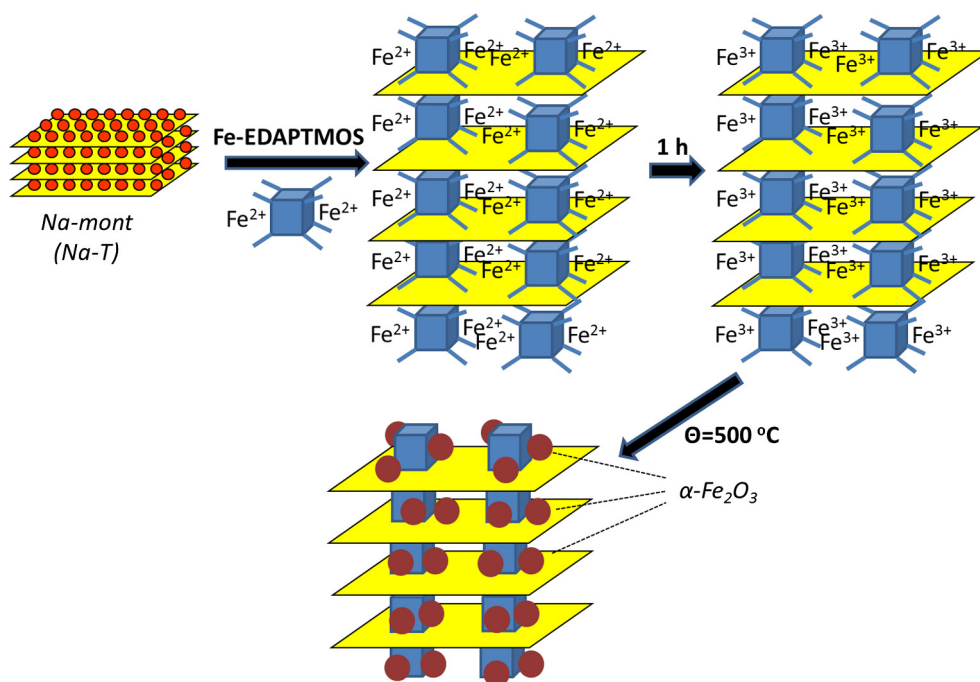

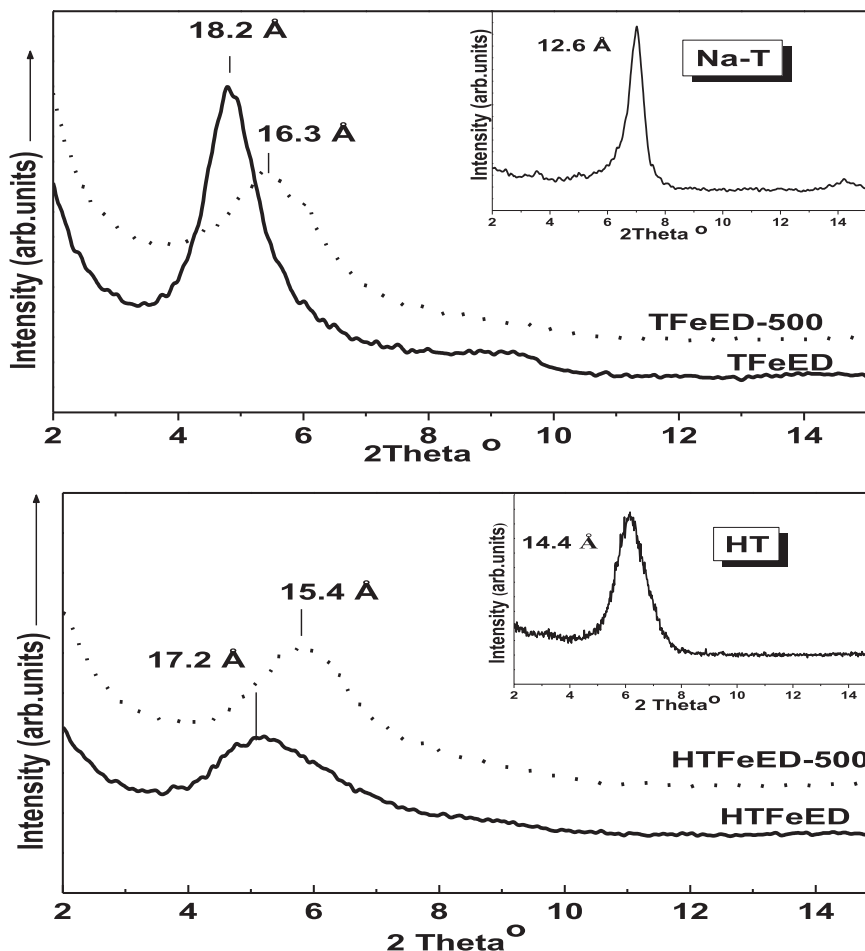Fig. 1. Schematic representation of experimental procedure.

Fig. 2. X-ray diffaction patterns of intercalated clay samples, **TFeED** and **HTFeED**, and the corresponding pillared structures produced upon calcination, **TFeED-500** (left) and **HTFeED-500** (right). Insets: pristine clays, **Na-T** and **HT**.

3.3. Infrared spectra

Fig. 3 shows the infrared spectra of the pristine acid activated clay (**HT**) and of **HTFeED** and **HTFeED-500**; the spectrum of the Fe-EDAPTMOS complex which was obtained as solid (orange) after the centrifugation of the complex solution during the synthetic procedure, is also shown. The infrared spectrum of **HT** consists of three absorption bands at lower frequencies (below 1300 cm^{-1}); the first, at 1000–1200 cm^{-1} corresponds to stretching vibrations of Si-O-M bridges (where M = Si, Al, Mg, Fe), the second one at 800–1000 cm^{-1} to libration modes of the OH groups of the octahedral layers and the third at 400–700 cm^{-1} to bending vibrations of the Si—O—Si and Si—O—Al bridges of the clay framework [46]. These same bands are also present in the spectrum of **HTFeED**. The NH$_2$ deformation of the aliphatic chains of the silicon cubes, expected at 1620 cm^{-1}, is superimposed on the broad band at 1650 cm^{-1}, which arises from the vibrations of interlayer water. Analogously the asymmetric stretching band of Si-O—Si linkages of the polysiloxane in the 1000–1200 cm^{-1} region (Fig. 3d) is not clearly distinguishable in the intercalated clay composites (Fig. 3b and c) due to the existence of the same type vibrations (Si—O—Si) of the clay framework in the same spectral region. The band at 690 cm^{-1} and the broad band at 1458 cm^{-1} observed in the spectrum of Fe-EDAPTMOS can be attributed to CH bending vibrations and NH wagging of the aliphatic chains of the EDAPTMOS cubes [14,15] respectively. The appearance of these bands in the spectrum of **HTFeED** is indicative of the insertion of

organosilicon cubes in the clay galleries. Both bands disappear upon calcination, as seen in the spectrum of **HTFeED-500**. Analoguous results were obtained for the samples based on sodium-montmorillonite, **Na-T**, **TFeED** and **TFeED-500** (see supporting information).

3.4. EPR analysis

EPR spectroscopy was used in order to shed light onto the origin and formation process of the iron-siloxane complex and the subsequent development of the pillared clay. Fig. 4A shows the EPR spectrum recorded at 4.2 K from an aqueous solution of FeCl$_2$ (0.5 mM). A broad signal whose lineshape and position are strongly reminiscent of signals arising from integer spin systems [50], is observed at low field values. This signal is readily assigned to Fe^{2+}(S = 2). Control experiments show that there is no change in the EPR spectrum after prolonged incubation at room temperature under ambient atmosphere [not shown]. Addition of EDAPTMOS in methanol (1.5 mM final concentration) results in a green solution whose EPR spectrum is shown in Fig. 4B. A decrease of the Fe^{2+}(S = 2) signal is observed; control experiments suggest that this decrease is partially due to methanol. New signals, namely a weak absorption feature at g $\sim$ 9.0 and a derivative like at g = 4.3, appear. These signals are characteristic for Fe^{3+}(S = 5/2) in rhombic environment. Moreover another signal with a peak at g = 1.93 can also be identified and probably arises from S = 1/2 species such as mixed valence iron dimers [51] presenting a small fraction of iron centers]. After
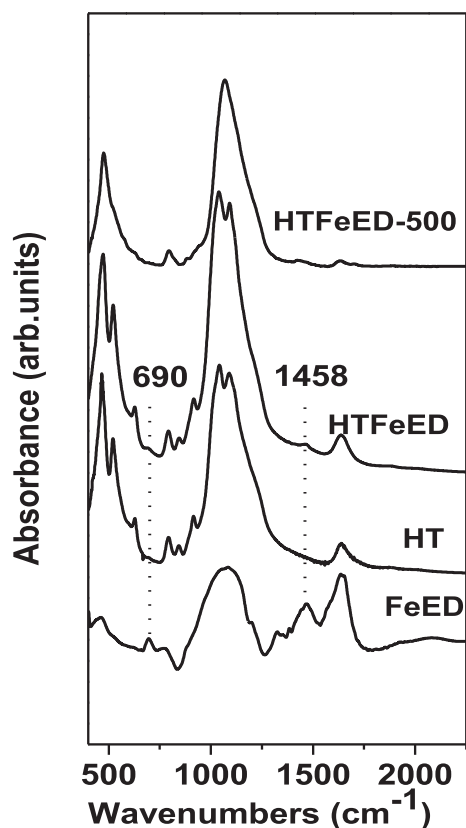
Fig. 3. FTIR spectra of pristine **HT**, **HTFeED** and **HTFeED-500**; the spectrum of the Fe-EDAPTMOS complex (FeED) is added for comparison.
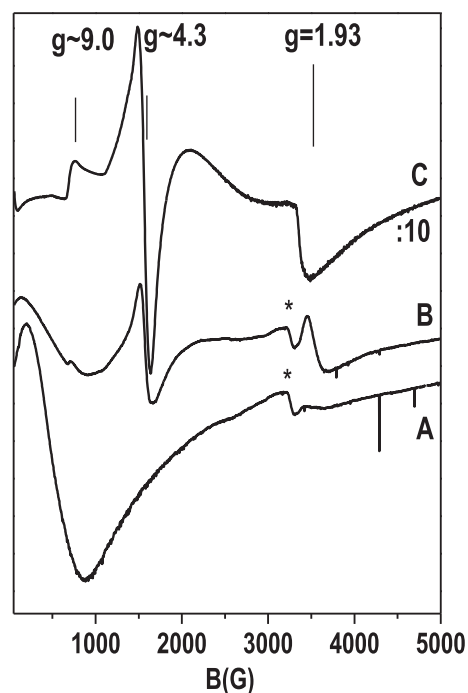

Fig. 4. A. EPR spectra from an aqueous solution of FeCl₂, B. immediately after addition of EDAPTMOS in methanol (1.5 mM final concentration) and C. after 2.5 h of stirring at ambient conditions. The asterisks indicate signals originating from impurities in the microwave cavity. *EPR conditions.* T, 4.2 K, microwave frequency, 9.38 mW, mod. amplitude, 25 G_{pp}.

Fig. 5. Room temperature EPR spectra from (A) **Na-T**, (B) the Fe-EDAPTMOS complex in the solid state, (C) same complex in solution, (D) **TFeED** unwashed, (E) **TFeED** washed three times with water, and (F) as E, after heat treatment at 500 °C (**TFeED-500**). EPR conditions: Mod. Amp. 25 Gpp, microwave power, 32 mW, microwave frequency 9.42 MHz.

2.5 h of stirring at ambient temperature the solution turns orange; the corresponding EPR spectrum is shown in 4C. The signal at low field values and the signal at g = 1.93 observed in Fig. 4A and B have disappeared and the g ∼ 9.0 and g = 4.3 signals show a ∼30-fold increase. A broad feature at g = 2.0 is also present. The overall spectral features are quite similar to those of several iron doped glasses [52,53]. Similar signals have been observed from zeolites doped with iron [54] and attributed to mononuclear species with the iron in the Fe^{3+}(S = 5/2) state. The g ∼ 9.0 and g = 4.3 signals represent sites with the ferric ion in a rhombic environment with substantial zero field splitting whereas the g = 2.0 signal represents centers where the environment around the ferric ion is more symmetric with negligible zero field splitting. The broadness of the latter points to distributions of the zero field splitting parameters of the iron, which in turn reflects a rather inhomogeneous environment around the paramagnetic ion [52–54].

Fig. 5A shows the EPR spectrum from the untreated clay. A signal at g ∼ 4.3 corresponds to Fe^{3+}(S = 5/2) species; this signal is very weak and represents a very small amount of iron impurities. Fig. 5B and C shows the spectra from the Fe-EDAPTMOS complex in the solid state and in solution respectively. The signals are rather different; we assume that the EPR properties in the solid state are governed by magnetic interactions between Fe^{3+}(S = 5/2) species, giving rise to the peak at g ∼ 2.4. Fig. 5D and E show the spectra of the clay after incorporation of the complex prior to and after washing respectively. A comparison with spectra 5B and 5E suggests that the complex in the clay gives rise to a signal similar with that of the complex in solution and not with that of the complex in the solid state. It is expected that the iron sites are well isolated inside the clay preventing thus from magnetic interactions. Moreover the environment of the iron remains symmetric. The signal at g ∼ 4.3 may suggest that during incorporation of the complex into the clay some iron sites undergo rhombic distortions. Finally, heat treatment at 500 K of the washed and unwashed clay samples leads to broad EPR signals (spectrum 5F) indicating the formation of oxides in agreement with Mössbauer results (see below).

Fig. 6. Mössbauer spectra of TFeED-500 (a) and HTFeED-500 (b) samples recorded at different temperatures.

Table 1

Mössbauer hyperfine parameters as resulting from the best fits of the Mössbauer spectra of the TFeED-500 and HTFeED-500 samples re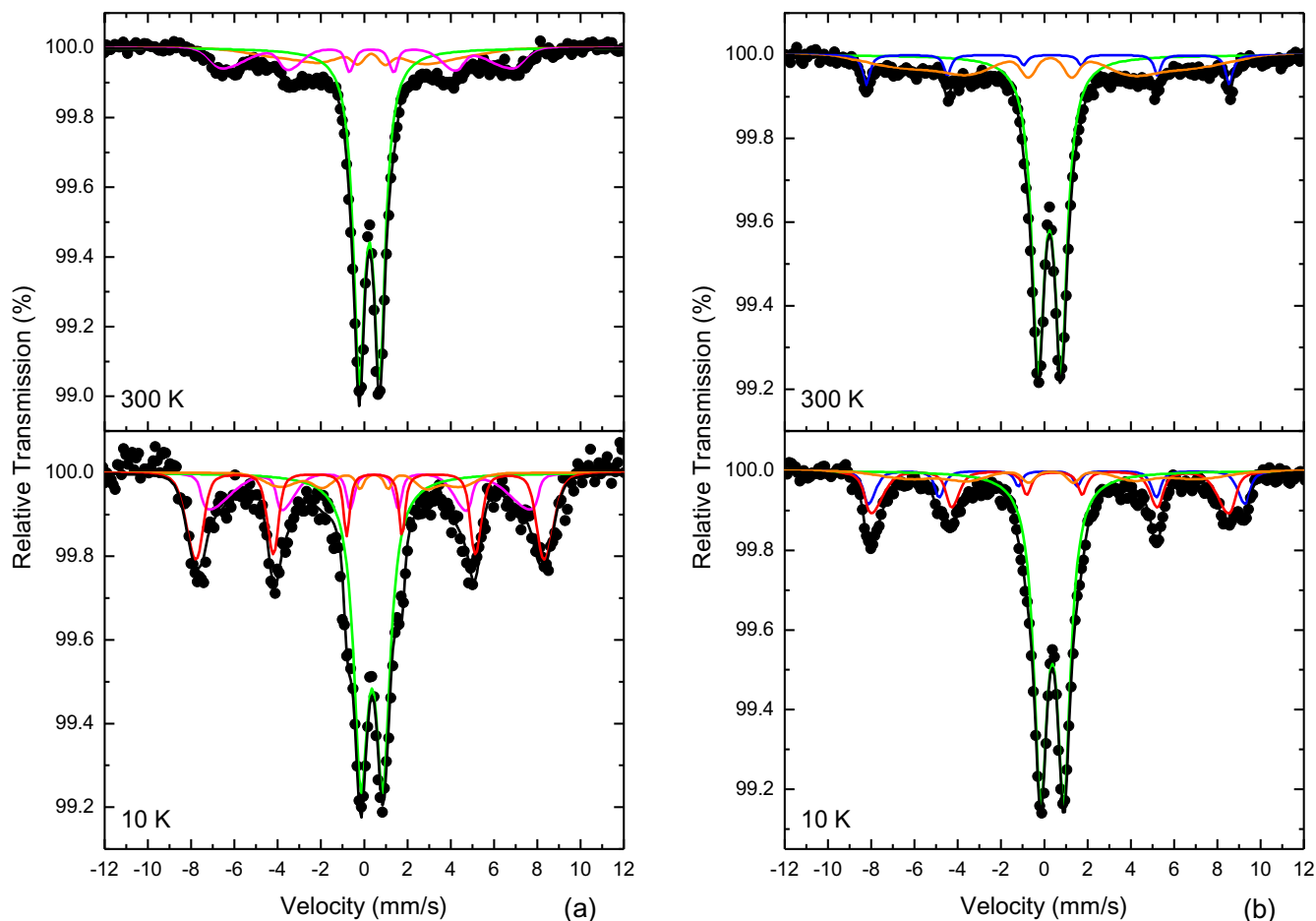corded at 300 K and 10 K. IS is the isomer shift (relative to a-Fe at 300 K), $\Gamma/2$ is the half line-width, QS is the quadrupole splitting, 2ε is the quadrupole shift, B_{hf} is the central value of the hyperfine magnetic field, ΔB_{hf} is the hyperfine magnetic field spreading (symmetric in single column, or asymmetric denoted by the < and > symbols in the relative columns) around B_{hf} and A is the relative spectral absorption area of the components used to fit the spectra. Typical errors are ±0.02 mm/s for IS, $\Gamma/2$, 2ε and QS, ±0.3 T for B_{hf} and ±5% for A.

Sample	T (K)	IS mm/s	$\Gamma/2$ mm/s	QS or 2ε mm/s	B_{hf} kOe	ΔB_{hf} kOe	$\Delta B_{hf} < B_{hf}$ kOe	$\Delta B_{hf} > B_{hf}$ kOe	Area %
TFeED-500	300	0.35	0.32	0.94	–	–	–	–	66
		0.35	0.14	−0.21	424	–	34	14	19
		0.35	0.14	−0.20	242	90	–	–	15
	10	0.47	0.40	1.02	–	–	–	–	48
		0.47	0.14	−0.20	257	43	–	–	8
		0.48	0.15	−0.20	497	–	7	12	26
		0.47	0.15	−0.21	482	–	34	0	18
HTFeED-500	300	0.35	0.35	1.06	–	–	–	–	66
		0.38	0.18	−0.21	521	3	–	–	7
		0.32	0.15	−0.10	392	108	–	–	27
	10	0.48	0.37	1.08	–	–	–	–	60
		0.48	0.20	0.41	541	–	10	0	10
		0.48	0.23	−0.20	528	–	16	0	19
		0.49	0.15	0.12	409	83	–	–	11

3.5. Mössbauer spectra

Fig. 6 shows typical Mössbauer spectra of the pillared hybrid materials after calcination at 500 °C. Both quadrupole and magnetically split components are observed in the spectra and their resonant lines possess some degree of broadening. In addition the absorption area of the magnetic components increases at 10 K relative to that observed at 300 K, at the expense of the area of the quadrupole split component. The IS, quadrupole splitting (QS), quadrupole shift (2ε) and hyperfine magnetic field (B_{hf}) values listed in Table 1, correspond to Fe^{3+} high spin (S = 5/2) ions in α-Fe_2O_3 (hematite) nanoparticles [55–57] These nanoparticles acquire a distribution of particle sizes and are subjected to superparamagnetic relaxation phenomena [58,59].
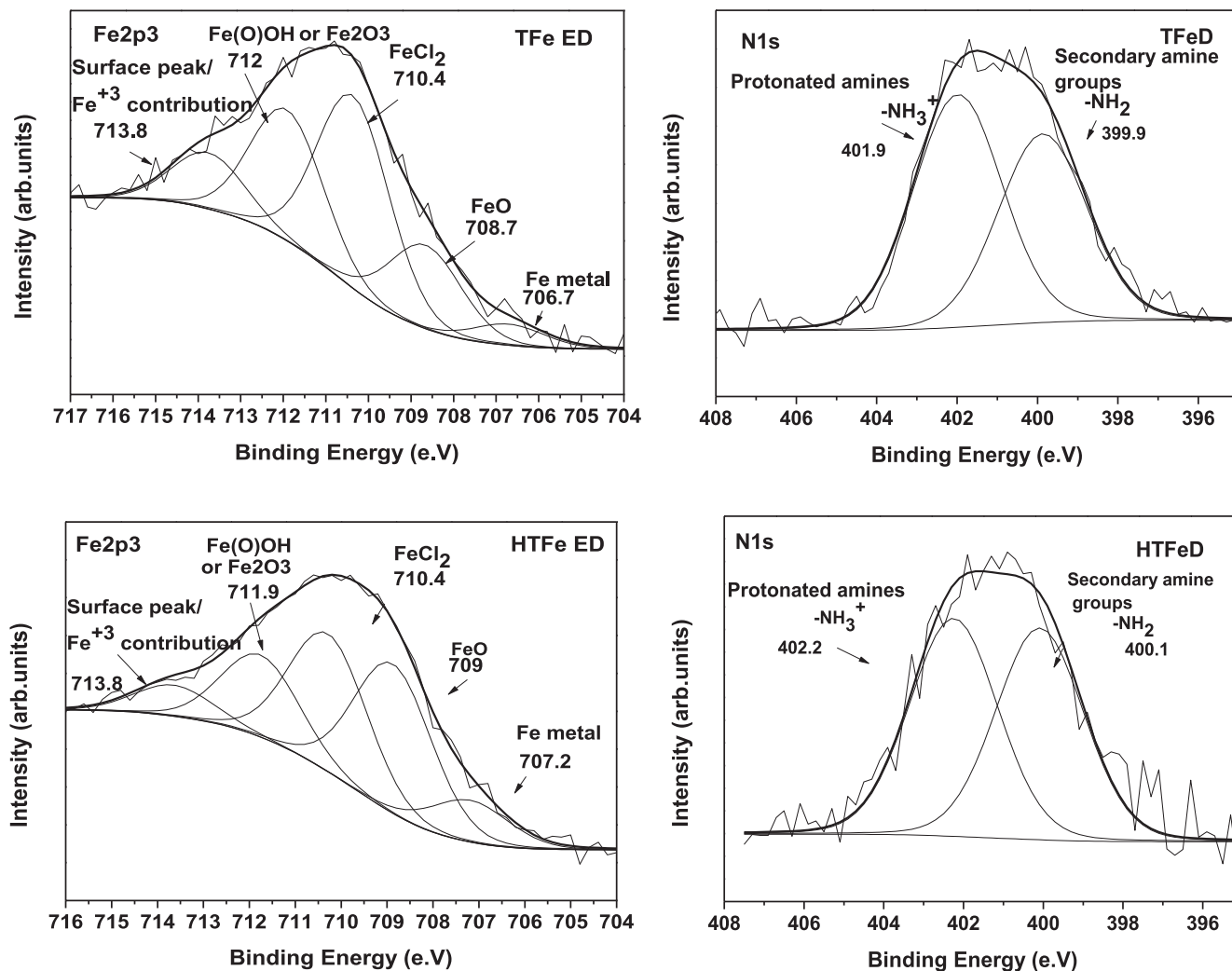
Fig. 7. X-ray photoemission spectra of the Fe2p3/2 (left) and N1s (right) core level regions of **TFeED** and **HTFeED.**
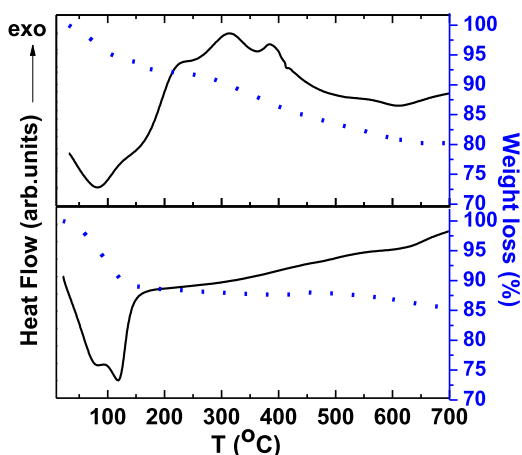

Fig. 8. DTA-TGA curves of pristine **HT** (bottom) and of **HTFeED** (top).

3.6. X-ray photoemission spectra

XPS spectroscopy was also used to identify the constituents of **TFeED** and **HTFeED** and to verify the successful incorporation of the iron complexes in the montmorillonite matrices. In every survey spectrum (see Supporting Information) iron peaks were observed at the expected binding energies (Fe2$p_{3/2}$ at 710 eV and Fe2$p_{1/2}$ at 723 eV). To identify which iron and nitrogen species are present we fitted the core level spectra shown in Fig. 7. In the case of iron we followed the approach of Grosvenor et al. [60]. For both **TFeED** and **HTFeED** five iron components are present, Fe(O)OH, FeCl$_2$ being the most dominant ones. Additionally, the nitrogen spectra reveal two nitrogen components, a first one peaked at around 402 eV binding energy, which accounts for 55% and 51% of the total N1s intensity for **TFeED** and **HTFeED** respectively, and which we attribute to protonated terminal amines of the silsesquioxane moieties and a second one at 400 eV, which makes up 45% and 51% of the total N1s intensity for **TFeED** and **HTFeED** respectively) and which is due to secondary amine groups of the same moieties [61]. Finally the intensity ratio silicon Si2p/ aluminum Al2s increased from 2.6 for **Na-T** to 4.9 and 4.5 for **TFeED** and **HTFeED** respectively. This increase is due to the extra silicon stemming from the incorporation of silsesquioxanes and confirms, together with the FTIR spectra and the XRD data discussed above, the successful intercalation of the iron complexes in the clay matrices.

3.7. Thermal analysis

Fig. 8 shows the DTA-TGA curves, of the intercalated hybrid **HTFeED** and of the pristine acid-activated montmorillonite, **HT**.

HT shows a 10% weight loss up to 120 °C, related to the removal of the intercalated water. The amount of adsorbed water is considerable lower (6 wt%) in the case of **HTFeED** revealing the less hydrophilic character of this hybrid structure. Moreover, **HTFeED** presents three exothermic peaks between 150 and 420 °C accompanied by an approximately 10% weight loss. Considering the mass percentage, these signals must correspond to the removal of the organic chains of the silsesquioxane cubes, which takes place in three exothermic steps. Consequently, considering an octahedral complex of the type $Fe_{8/3}^{3+}[X_8Si_8O_{12}]$, where X is $H_2N(CH_3)_2NH(CH_2)_3$-, the amount of Fe-EDAPTMOS incorporated within the clay is estimated to account for 17% of the total mass. Analogous results were obtained for **TFeED**. In this case, the organic part of intercalated moieties was found to correspond to about 15 wt% of the total mass (see Supporting Information) and thus the percentage of the organosilicon cubes to about 25 wt%.

3.8. Surface area and porosity measurements – a_s plots

Nitrogen adsorption-desorption measurements (at 77K) were performed on both pillared clays in order to determine the porosity in each case. We not only obtained the specific-surface-areas (S_{BET}) obtained from the isotherms through BET analysis, but, in order to distinguish between the external plus mesoporous surface area and micropore volume, we also made use of the a_s-plot method [62,63]. The a_s plots, defined as $a_s = (n_s/n_{0.4})_{ref}$ where n_s, $n_{0.4}$ are the amounts of N_2 adsorbed by a reference solid at $P/P_o = s$ and $P/P_o = 0.4$, have been proposed [62,63] as a very valuable tool to investigate the porosity of solids. According to Gregg and Sing [62] it is convenient to set $a_s = 1$ at $P/P_o = 0.4$, since monolayer coverage and microporous filling occur at $P/P_o < 0.4$, while capillary condensation takes place at $P/P_o > 0.4$. In the present study two treatments with two different reference solids were carried out. As reference material **Na-T,** heated at 800 °C for 3 h to eliminate the pores, with a specific surface area of 5 $m^2\,g^{-1}$ was employed. The slope of the linear part of the V-a_s plot gives the meso+external surface area, $S_{m,e} = 2.87 \times V_{ads}/a_s$, while the positive intercept gives the microporous volume, $V_{\mu p}$, after conversion of the gas volume adsorbed at 77 K: $V_{\mu p} = V_{ads}(STP) \times 0.001547$.

The values of specific surface area (S_{BET}) and total pore volume (V_p) from the experimental measurements as well as the mesoporous plus external surface ($S_{m,e}$), the micropores volume ($V_{\mu p}$) and micropores surface area ($S_{\mu p}$) calculated as described above are reported in Table 2.

As obvious from the values of Table 2, the BET specific surface area (S_{BET}) of the pristine clay increased after the acid activation. In addition **TFeED-500** and **HTFeED-500** hybrids show a significant increase in S_{BET} as compared to the pristine clay materials. More specifically the S_{BET} of **TFeED-500**, 248 $m^2\,g^{-1}$, amounts to 4 time the value of **Na-T** (61 $m^2\,g^{-1}$) while in the case of **HTFeED-500** the S_{BET} was almost double (230 $m^2\,g^{-1}$ as compared to 107 $m^2\,g^{-1}$ for **HT**). Moreover $S_{m,e}$ also increased for the intercalated hybrids (in the case of **TFeED-500** $S_{m,e}$ doubled) while the

values of $V_{\mu p}$ for both hybrids (0.068 $cm^3\,g^{-1}$ for **TFeED-500** and 0.061 $cm^3\,g^{-1}$ for **HTFeED-500**) are indicative of pillared structures.

3.9. Isopropanol decomposition

The decomposition of isopropanol is considered an acid catalyzed reaction, which is affected by the number and strength of the active acid sites on the surface of the pillared clays. The acid activation treatment as well as the presence of iron oxides bonded on the pillars of the system enhance the acidic character and result in the improvement of the catalytic properties [64–66]. The total degrees of conversion of isopropanol (Fig. 9a) as well as the selectivity towards propene and diisopropylether (Fig. 9b) are depicted as a function of reaction temperature. The data in Fig. 9(a) clearly indicate that both samples show a high catalytic activity due to the presence of acid sites on the surface. Since the decomposition of isopropanol is an acid catalyzed reaction, which is favored by catalysts with large number of acid sites, it is not surprising that **HTFeED-500**, which has been prepared using as starting material acid-activated clay, shows a higher activity. Moreover, as evidenced from Fig. 9(b) the selectivity to diisopropylether of **TFeEDW-500** slightly predominates the selectivity to propene up to 105 °C, while in the case of **HTFeED-500**, the selectivity to propene starts from the values around 75%, and remains constant up to 105 °C.

Generally, the product profiles show that both propene and diisopropylether are present from the onset of the reaction, indicating that both reaction products are formed by direct dehydration; i.e., they are primary reaction products coming from isopropanol through a parallel reaction network. According Campelo et al. [67] the pathway of formation of both products from 2-propanol conversion on $AlPO_4$ catalysts is a combination pathway of parallel and consecutive reactions (Fig. 10).

Therefore, propene is a primary plus secondary reaction product while diisopropylether is a primary unstable product. In our case, it is clear that for all samples, the production of propene predominates at high reaction temperature and reaches 100% above 130 °C, independently of how many intermediates may be involved in its formation. On the other hand the differentiation on the onset selectivity to diisopropylether for the examined samples might be connected to stereochemical parameters. Thus the selectivity for the larger product (diisopropylether) is favoured on the catalyst with higher d-spacing (**TFeED-500**).

Acid activation of clays is performed to enhance their catalytic activity [68]; after the treatment with surfactants in order to modify the clay's surface area the conversion of isopropanol is 5.29% at 120 °C [69]. After acid activation the conversion percentage can instead reach 50% at 180 °C, as reported by Yavad et al. [70]. As shown by Trombetta et al. [71], in the case of acid pillared clays the conversion percentage can reach 49.4% – a value that is lower than what we report for our catalysts. 100% conversion is also reported, but at significantly higher temperatures (450 °C) [72]. On the other hand other similar systems like γ-Al_2O_3 [73] can

Table 2
Results from a_s analysis, using as reference material **Na-T,** heated to 800 °C to eliminate the pores.

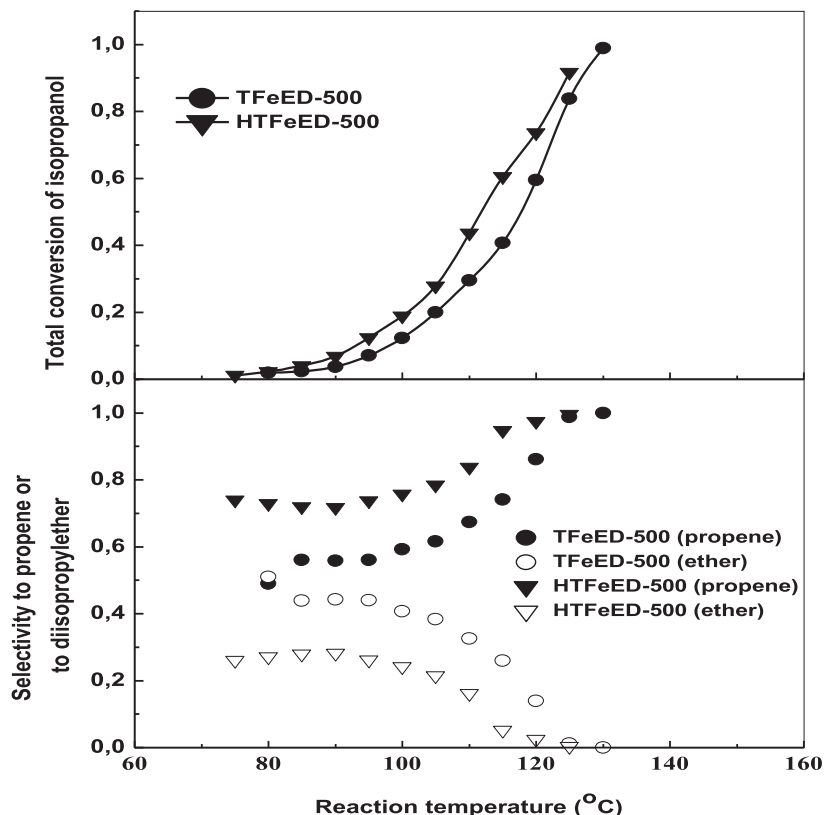| Sample	$S_{BET}(m^2g^{-1})$	V_p (cm^3g^{-1})	$S_{m,e}$ (m^2g^{-1})	$V_{\mu p}$ (cm^3g^{-1})	100 ($S_{m,e}/S_{BET}$)%	100 ($V_{\mu p}/V_p$) %
TFeED-500	248.8	0.256	107.4	0.068	43.2	26.6
HTFeED-500	230.2	0.263	102.7	0.061	44.6	23.2
HT	107.8	0.151	67.3	0.022	62.4	14.6
Na-T	61	0.126	54.8	0.006	89.8	4.8

Fig. 9. (a) The total degrees of conversion of isopropanol and (b) the selectivity towards propene (dark symbols) and diisopropylether (open symbols) as a function of reaction temperature for **TFeED-500** and **HTFeED-500** pillared clays.
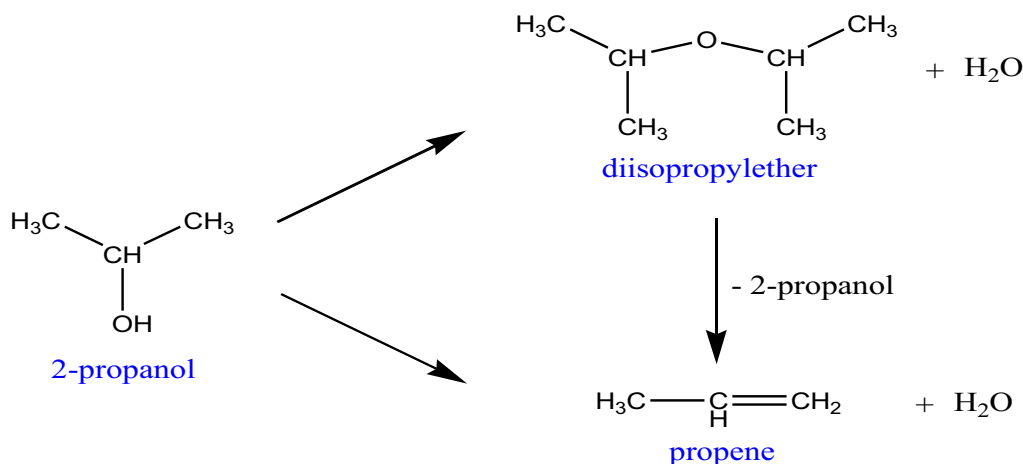

Fig. 10. Reaction network during the decomposition of isopropanol.

reach a 35% conversion percentage at 200 °C, while metal oxides convert 65% of the isopropanol [74] or even 80% if the reaction takes place in temperature above 160 °C [36].

4. Conclusions

Intercalation of Fe^{3+}-substituted cubic silsesquioxanes in layered aluminosilicate nanoclays resulted in the formation of novel catalytic pillared structures. Octameric cubic oligosiloxanes, formed upon controlled hydrolytic polycondensation of the corresponding bi-functional amino-silane monomer (EDAPTMOS), were reacted with iron cations to form iron-siloxane complexes. These cationic complexes were intercalated in a sodium and an acid activated nanoclay and the resulting intercalated structures were further calcined to remove the organic side arms and produce crosslinked metal-substituted silica-pillared clays of high porosity and thermal stability. XRD measurements revealed the successful intercalation of iron-silsesquioxane complexes within the clay interlayers as well as the formation of the pillared structures upon calcination. The absence of reflection peaks of the crystalline phase of iron oxides indicates that iron oxide nanoparticles produced upon calcination are small enough and are not aggregated on the external clay surfaces but rather homogeneously dispersed in

the clay matrix. The incorporation of the organosilicon cubes in the clay galleries was confirmed by infrared and X-ray photoelectron spectroscopies while EPR analysis shed light onto the origin and formation process of the iron-siloxane complex used as the pillaring solution and the subsequent development of the pillared clay. The amount of the iron-silicon cubane complexes incorporated within the clay was estimated by thermal analysis between 17% and 25% of the total mass. Mössbauer spectra of the pillared materials after calcination at 500 °C, in agreement with EPR analysis, showed the existence of α-Fe_2O_3 (hematite) nanoparticles in the final hybrid systems. Nitrogen adsorption-desorption measurements showed that the specific surface area (S_{BET}) of the calcined intercalated clays was increased up to four times compared with that of pristine clays while the pore characteristics as estimated by the a_s-plot method are indicative of pillared structures. Finally, pillared clays showed high acid catalytic activity for isopropanol decomposition due to the presence of acid sites on the surface. In fact, pillared clay prepared using acid-activated clay as starting material showed a higher activity due to the large number of acid sites. The selectivity to diisopropylether of the pillared clay prepared from sodium-clay, slightly predominates the selectivity to propene up to 105 °C, while in the case of acid activated pillared clay, the selectivity to propene starts from the values around 75%, and remained constant up to 105 °C. This differentiation on the onset selectivity is a to stereochemical parameters. The resulting pillared clays exhibiting high specific areas and narrow pore size distribution could also be used as catalysts in many catalytic reactions in organic synthesis.

Acknowledgements

Appendix A. Supplementary material

Supplementary data associated with this article can be found, in the online version, at http://dx.doi.org/10.1016/j.jcis.2017.09.003.

References

[1] A. Sellinger, R.M. Laine, Silsesquioxanes as synthetic platforms. 3. Photocurable, liquid epoxides as inorganic/organic hybrid precursors, Chem. Mater. 8 (8) (1996) 1592–1593.

[2] A. Sellinger, R.M. Laine, Silsesquioxanes as synthetic platforms. thermally curable and photocurable inorganic/organic hybrids, Macromolecules 29 (6) (Jan. 1996) 2327–2330.

[3] G. Potsi et al., Carbon nanostructures containing polyhedral oligomeric silsesquioxanes (POSS), Curr. Org. Chem. 20 (6) (2016) 662–673.

[4] D.B. Cordes, P.D. Lickiss, F. Rataboul, Recent developments in the chemistry of cubic polyhedral oligosilsesquioxanes, Chem. Rev. 110 (4) (2010) 2081–2173.

[5] Y. Kaneko, E.B. Coughlin, T. Gunji, M. Itoh, K. Matsukawa, K. Naka, Silsesquioxanes: recent advancement and novel applications, Int. J. Polym. Sci., 2012, p. 2.

[6] D.W. Scott, Thermal rearrangement of branched-chain methylpolysiloxanes1, J. Am. Chem. Soc. 68 (3) (1946) 356–358.

[7] S.H. Phillips, T.S. Haddad, S.J. Tomczak, Developments in nanoscience: polyhedral oligomeric silsesquioxane (POSS)-polymers, Curr. Opin. Solid State Mater. Sci. 8 (1) (2004) 21–29.

[8] R. Tamaki, Y. Tanaka, M.Z. Asuncion, J. Choi, R.M. Laine, Octa(aminophenyl) silsesquioxane as a nanoconstruction site, J. Am. Chem. Soc. 123 (49) (2001) 12416–12417.

[9] R.M. Laine, J. Choi, I. Lee, Organic–inorganic nanocomposites with completely defined interfacial interactions, Adv. Mater. 13 (11) (2001) 800–803.

[10] C. Zhang, T.J. Bunning, R.M. Laine, Synthesis and characterization of liquid crystalline silsesquioxanes, Chem. Mater. 13 (10) (Oct. 2001) 3653–3662.

[11] C. Zhang et al., Highly porous polyhedral silsesquioxane polymers. Synthesis and characterization, J. Am. Chem. Soc. 120 (33) (1998) 8380–8391.

[12] R.M. Laine, M.F. Roll, Polyhedral phenylsilsesquioxanes, Macromolecules 44 (5) (2011) 1073–1109.

[13] W.J. Yao Min Gu Xueping, Feng Lianfang, Synthesis and application of dendrimers based on polyhedral oligomeric silsesquioxanes, Prog. Chem. 24 (203) (2012) 405–413.

[14] A. Szabó, D. Gournis, M.A. Karakassides, D. Petridis, Clay–aminopropylsiloxane compositions, Chem. Mater. 10 (2) (Feb. 1998) 639–645.

[15] D. Petridis, D. Gournis, M.A. Karakassides, The chemistry of organofunctionalized silicon cubanes in swelling smectites, Mol. Crys. Liq. Crys. Sci. Technol. Section A Mol. Cryst. Liq. Cryst. 311 (1) (Mar. 1998) 345–350.

[16] G. Fetter, D. Tichit, P. Massiani, R. Dutartre, F. Figueras, Preparation and characterization of montmorillonites pillared by cationic silicon species, Clays Clay Miner. 42 (2) (1994) 161–169.

[17] L.M. Johnson, T.J. Pinnavaia, Hydrolysis of (γ-aminopropyl)triethoxysilane-silylated imogolite and formation of a silylated tubular silicate-layered silicate nanocomposite, Langmuir 7 (11) (1991) 2636–2641.

[18] J. Ahenach, P. Cool, E. Vansant, O. Lebedev, J. Van Landuyt, Influence of water on the pillaring of montmorillonite with aminopropyltriethoxysilane, Phys. Chem. Chem. Phys. 1 (15) (1999) 3703–3708.

[19] R.M. Barrer, Expanded clay minerals: a major class of molecular sieves, J. Inclus. Phenom. 4 (2) (1986) 109–119.

[20] J. Roziere, D.J. Jones, T. Cassagneau, Crosslinked layered materials formed by intercalation of octameric siloxanes in metal(IV) hydrogen phosphates, J. Mater. Chem. 1 (6) (1991) 1081–1082.

[21] T. Cassagneau, D.J. Jones, J. Roziere, Novel inorganic oxide pillared.gamma.-zirconium phosphate formed by intercalation of octameric siloxanes, J. Phys. Chem. 97 (34) (Aug. 1993) 8678–8680.

[22] P. Olivera-Pastor et al., Nanostructured inorganically pillared layered metal(IV) phosphates, Chem. Mater. 8 (8) (1996) 1758–1769.

[23] W. Hou, J. Ma, Q. Yan, X. Fu, Highly thermostable, porous, layered titanoniobate pillared by silica, J. Chem. Soc., Chem. Commun. 14 (1993) 1144–1145.

[24] D.R. Dreyer, S. Park, C.W. Bielawski, R.S. Ruoff, The chemistry of graphene oxide, Chem. Soc. Rev. 39 (1) (2010) 228–240.

[25] A.B. Bourlinos, D. Gournis, D. Petridis, T. Szabo, A. Szeri, I. Dekany, Graphite oxide: chemical reduction to graphite and surface modification with primary aliphatic amines and amino acids, Langmuir 19 (15) (2003) 6050–6055.

[26] A. Gomathi, K. Gopalakrishnan, C.N.R. Rao, Covalent functionalization of metal oxide and carbon nanostructures with polyoctasilsesquioxane (POSS) and their incorporation in polymer composites, Mater. Res. Bull. 45 (12) (Dec. 2010) 1894–1898.

[27] X. Shen, Y. Cui, Y. Pang, H. Qian, Graphene oxide nanoribbon and polyhedral oligomeric silsesquioxane assembled composite frameworks for pre-concentrating and electrochemical sensing of 1-hydroxypyrene, Electrochim. Acta 59 (Jan. 2012) 91–99.

[28] S. Jana, S. Das, Development of novel inorganic-organic hybrid nanocomposites as a recyclable adsorbent and catalyst, Rsc Adv. 4 (65) (2014) 34435–34442.

[29] S. Kataoka et al., Layered hybrid perovskites with micropores created by alkylammonium functional silsesquioxane interlayers, J. Am. Chem. Soc. 137 (12) (Apr. 2015) 4158–4163.

[30] G. Balomenou, P. Stathi, A. Enotiadis, D. Gournis, Y. Deligiannakis, Physicochemical study of amino-functionalized organosilicon cubes intercalated in montmorillonite clay: H-binding and metal uptake, J. Colloid Interface Sci. 325 (1) (Sep. 2008) 74–83.

[31] U. Flessner et al., A study of the surface acidity of acid-treated montmorillonite clay catalysts, J. Mol. Catal. A, Chem. 168 (1–2) (2001) 247–256.

[32] A.K. Ladavos et al., Synthesis, characterization and catalytic activity of LayMOx (M=Ni, Co) perovskite-type particles intercalated in clay via heterobinuclear complexes, Appl. Clay Sci. 13 (1) (Jun. 1998) 49–63.

[33] V.N. Stathopoulos, A.K. Ladavos, K.M. Kolonia, S.P. Skaribas, D.E. Petrakis, P.J. Pomonis, Preparation, characterization and surface acid catalytic activity of microporous clays pillared with Al1−xFexOy (x=0.00 to 1.00) oxidic species, Micropor. Mesopor. Mater. 31 (1–2) (Oct. 1999) 111–121.

[34] A.K. Ladavos, P.N. Trikalitis, P.J. Pomonis, Surface characteristics and catalytic activity of Al-Pillared (AZA) and Fe-Al-pillared (FAZA) clays for isopropanol decomposition, J. Mol. Catal. A: Chem. 106 (3) (1996) 241–254.

[35] F. Tomul, Adsorption and catalytic properties of Fe/Cr-pillared bentonites, Chem. Eng. J. 185–186 (Mar. 2012) 380–390.

[36] R. Issaadi, F. Garin, C.-E. Chitour, Study of the acid character of some palladium-modified pillared clay catalysts: use of isopropanol decomposition as test reaction, Catal. Today 113 (3–4) (Apr. 2006) 166–173.

[37] F. Khattou, G. Aptel, J.-V. Zanchetta, D.J. Jones, B. Deroide, J. Roziere, Use of a Cu^{2+} probe to characterise silica-pillaring in zirconium phosphate by electron paramagnetic resonance spectroscopy, J. Mater. Chem. 9 (10) (1999) 2453–2458.

[38] F. Khattou, G. Aptel, D.J. Jones, B. Deroide, J. Rozière, J.-V. Zanchetta, Characterisation of calcined silica-pillared zirconium phosphate: a Cu^{2+} e.p.r. study, Micropor. Mesopor. Mater. 47 (2–3) (Oct. 2001) 231–241.

[39] F. Carniato et al., Titanosilsesquioxanes embedded in synthetic clay as a hybrid material for polymer science, Angew. Chem. 121 (33) (Aug. 2009) 6175–6177.

[40] F. Carniato, C. Bisio, G. Gatti, M. Guidotti, L. Sordelli, L. Marchese, Organic-inorganic hybrid saponites obtained by intercalation of titano-silsesquioxane, Chem. Asian J. 6 (3) (2011) 914–921.

[41] F.A. He, L.M. Zhang, Using inorganic POSS-modified laponite clay to support a nickel alpha-diimine catalyst for in situ formation of high performance polyethylene nanocomposites, Nanotechnology 17 (24) (2006) 5941–5946.

[42] C. Pereira, A.R. Silva, A.P. Carvalho, J. Pires, C. Freire, Vanadyl acetylacetonate anchored onto amine-functionalised clays and catalytic activity in the epoxidation of geraniol, J. Mol. Catal. a-Chem. 283 (1–2) (2008) 5–14.

[43] J. Liang, Q. Zhang, H. Wu, G. Meng, Q. Tang, Y. Wang, Iron-based heterogeneous catalysts for epoxidation of alkenes using molecular oxygen, Catal. Commun. 5 (11) (2004) 665–669.

[44] D. Gournis, A. Lappas, M.A. Karakassides, D. Többens, A. Moukarika, A neutron diffraction study of alkali cation migration in montmorillonites, Phys. Chem. Miner. 35 (1) (2008) 49–58.

[45] C.N. Rhodes, D.R. Brown, Autotransformation and ageing of acid-treated montmorillonite catalysts: a solid-state 27Al NMR study, J. Chem. Soc., Faraday Trans. 91 (6) (1995) 1031–1035.

[46] P. Falaras, F. Lezou, Electrochemical behavior of acid activated montmorillonite modified electrodes, J. Electroanal. Chem. 455 (1–2) (Sep. 1998) 169–179.

[47] A. Douvalis, A. Polymeros, T. Bakas, IMSG09: A 57 Fe- 119 Sn Mössbauer spectra computer fitting program with novel interactive user interface, J. Phys: Conf. Ser. 217 (1) (2010) 12014.

[48] D. Briggs, M.P. Seah, Practical Surface Analysis by Auger and X-ray Photoemission spectroscopy, John Wiley & Sons Ltd., Chichester, 1983.

[49] B.K.G. Theng, The Chemistry of Clay Organic Reactions, Adam Hilger, London, 1974.

[50] M.P. Hendrich, P.G. Debrunner, Integer-spin electron paramagnetic resonance of iron proteins, Biophys. J. 56 (3) (Sep. 1989) 489–506.

[51] P.M. Hanna, Y. Chen, N.D. Chasteen, Initial iron oxidation in horse spleen apoferritin. Characterization of a mixed-valence iron(II)-iron(III) complex, J. Biol. Chem. 266 (2) (Jan. 1991) 886–893.

[52] C. Legein, J. Buzare, B. Boulard, C. Jacoboni, Short-range order quantification in transition metal fluoride glasses (TMFG) through EPR spectra simulation, J. Phys.: Condens. Matter 7 (25) (1995) 4829.

[53] J. Kliava, R. Berger, Y. Servant, J. Emery, J.M. Grenèche, J. Trokšs, Electron paramagnetic resonance and Mössbauer effect studies in iron-doped 57Fe isotope enriched phosphate glasses, J. Non-Cryst. Solids 202 (3) (Jul. 1996) 205–214.

[54] D. Goldfarb, M. Bernardo, K.G. Strohmaier, D.E.W. Vaughan, H. Thomann, Characterization of iron in zeolites by X-band and Q-band ESR, pulsed ESR, and UV-visible Spectroscopies, J. Am. Chem. Soc. 116 (14) (Jul. 1994) 6344–6353.

[55] W. Kündig, H. Bömmel, G. Constabaris, R.H. Lindquist, Some properties of supported small α–Fe_2O_3 particles determined with the Mössbauer effect, Phys. Rev. 142 (2) (Feb. 1966) 327–333.

[56] F. Bødker, M.F. Hansen, C.B. Koch, K. Lefmann, S. Mørup, Magnetic properties of hematite nanoparticles, Phys. Rev. B 61 (10) (2000) 6826–6838.

[57] F. Mørup, S. Bødker, Size dependence of the properties of hematite nanoparticles, EPL (Europhys. Lett.) 52 (2) (2000) 217.

[58] J.-M. Greneche, The Contribution of 57Fe Mössbauer spectrometry to investigate magnetic nanomaterials, in: Y. Yoshida, G. Langouche (Eds.), Mössbauer Spectroscopy: Tutorial Book, Springer Berlin Heidelberg, Berlin, Heidelberg, 2013, pp. 187–241.

[59] T. Tsoufis et al., Novel nanohybrids derived from the attachment of FePt nanoparticles on carbon nanotubes, J. Nanosci. Nanotechnol. 8(11) 5942–5951.

[60] A.P. Grosvenor, B.A. Kobe, M.C. Biesinger, N.S. McIntyre, Investigation of multiplet splitting of Fe 2p XPS spectra and bonding in iron compounds, Surf. Interface Anal. 36 (12) (2004) 1564–1574.

[61] X. Song, Y. Ma, C. Wang, P.M. Dietrich, W.E.S. Unger, Y. Luo, Effects of protonation, hydrogen bonding, and photodamaging on X-ray spectroscopy of the amine terminal group in aminothiolate monolayers, J. Phys. Chem. C 116 (23) (2012) 12649–12654.

[62] S.J. Gregg, K.S.W. Sing, Adsorption, surface area, and porosity TT-, second ed. Academic Press, London.

[63] A. Lecloux, J.P. Pirard, The importance of standard isotherms in the analysis of adsorption isotherms for determining the porous texture of solids, J. Colloid Interface Sci. 70 (2) (1979) 265–281.

[64] G. Connell, J.A. Dumesic, The generation of Brønsted and Lewis acid sites on the surface of silica by addition of dopant cations, J. Catal. 105 (2) (1987) 285–298.

[65] F. Trejo, M.S. Rana, J. Ancheyta, Genesis of acid–base support properties with variations of preparation conditions: cumene cracking and its kinetics, Ind. Eng. Chem. Res. 50 (5) (Mar. 2011) 2715–2725.

[66] K. Lázár, I. Manninger, B.M. Choudary, Associated and single iron ions in ion-exchanged faujasite zeolites, Hyperfine Interact. 69 (1) (1992) 747–750.

[67] J.M. Campelo, A. Garcia, J.F. Herencia, D. Luna, J.M. Marinas, A.A. Romero, Conversion of alcohols (α-methylated series) on $ALPO_4$ catalysts, J. Catal. 151 (2) (1995) 307–314.

[68] G.A. Mills, J. Holmes, E.B. Cornelius, The acid activation of some bentonite clays, J. Phys. Colloid Chem. 54 (8) (1950) 1170–1185.

[69] Y.Z. Yao, S. Kawi, Surfactant-treated K10 montmorillonite: a high-surface-area clay catalyst, J. Porous Mater. 6 (1) (1999) 77–85.

[70] G.D. Yadav, S.B. Kamble, Alkylation of xylenes with isopropyl alcohol over acidic clay supported catalysts: efficacy of 20% w/w $Cs_{2.5}H_{0.5}PW_{12}O_{40}$/K-10 clay, Ind. Eng. Chem. Res. 48 (21) (Nov. 2009) 9383–9393.

[71] M. Trombetta et al., Solid acid catalysts from clays, Appl. Catal. A 193 (1) (2000) 55–69.

[72] M. Raimondo, A. De Stefanis, G. Perez, A.A.G. Tomlinson, PLS vs. zeolites as sorbents and catalysts. 5. Evidence for Brønsted/Lewis acid crossover and high acidity in conversions of C1–3 alcohols in some alumina-pillared smectite clays, Appl. Catal. A 171 (1) (1998) 85–97.

[73] K. Larmier et al., Influence of coadsorbed water and alcohol molecules on isopropyl alcohol dehydration on γ-alumina: multiscale modeling of experimental kinetic profiles, ACS Catal. 6 (3) (2016) 1905–1920.

[74] J. Gaálová et al., Metal Mixed Oxides and Zeolites in Oxidation of Ethanol and Isopropanol, in: Proceedings of the 2014 International Conference on Chemical Engineering and Materials Science (CEMS '14), 2014.